

# Performance of the hybrid externally occulted *Lyot* solar coronagraph

## Application to ASPIICS

R. Rougeot<sup>1</sup>, R. Flamary<sup>2</sup>, D. Galano<sup>1</sup>, and C. Aime<sup>2</sup>

<sup>1</sup> European Space Research and Technology Center, European Space Agency, Keplerlaan 1, 2201 Noordwijk, The Netherlands  
e-mail: raphael.rougeot@esa.int

<sup>2</sup> Laboratoire Lagrange, Université Côte d'Azur, Centre National de la Recherche Scientifique, Observatoire de la Côte d'Azur, Parc Valrose, 06108 Nice, France

Received 6 July 2016 / Accepted 30 November 2016

### ABSTRACT

**Context.** High-contrast hybrid coronagraphs, which combine an external occulter and a *Lyot*-style coronagraph became a reality in recent years, despite the lack of analytic and numerical end-to-end performance studies. The solar coronagraph ASPIICS which will fly on the future ESA Formation Flying mission Proba-3 is a good example of such a hybrid coronagraph.

**Aims.** We aim to provide a numerical model to compute theoretical performance of the hybrid externally occulted *Lyot*-style coronagraph, which we then aim to compare to the performance of the classical *Lyot* coronagraph and the externally occulted solar coronagraph. We will provide the level and intensity distribution of the stray light, when the Sun is considered as an extended source. We also investigate the effect of different sizes for the internal occulter and *Lyot* stop.

**Methods.** First, we have built on a recently published approach, to express the diffracted wave front from Fresnel diffraction produced by an external occulter at the entrance aperture of the coronagraph. Second, we computed the coherent propagation of the wave front coming from a given point of the Sun through the instrument. This is performed in three steps: from the aperture to the image of the external occulter, where the internal occulter is set, from this plane to the image of the entrance aperture, where the *Lyot* stop is set, and from there to the final image plane. Making use of the axis-symmetry, we considered wave fronts originating from one radius of the Sun and we circularly average the intensities. Our numerical computation used the parameters of ASPIICS.

**Results.** The hybrid externally occulted *Lyot* coronagraph rejects sunlight below  $10^{-8} B_{\odot}$  from  $1.3 R_{\odot}$  – in the particular configuration of ASPIICS. The *Lyot* coronagraph effectively complements the external occultation. We show that reducing the *Lyot* stop allows a clear gain in rejection, being even better than oversizing the internal occulter, that tends to exclude observations very close to the solar limb. As an illustration, we provide a graph that allows us to estimate performance as a function of the internal occulter and *Lyot* stop sizes.

**Conclusions.** Our work consists of a methodological approach to compute the end-to-end performance for solar coronagraph.

**Key words.** Sun: corona – instrumentation: high angular resolution – methods: analytical

## 1. Introduction

The Sun's corona consists of a fully ionized plasma, with a strong magnetic field. Its physical structure and dynamics are governed by multiple processes, theoretical models of which still need to be assessed and investigated. Indeed, its properties, such as density of the plasma, temperature, and magnetic field structures, are far more complex than any other planet magnetosphere, as described by [Aschwanden \(2005\)](#). Coronal mass ejections (CMEs), heating processes operating in the corona, and even solar wind interaction and acceleration are still not perfectly understood. The active study of the corona of the Sun needs both simultaneous and complementary multi-wavelength observations. A very high angular resolution, of the order of the arcsecond, is required to constrain the finest coronal structures ([Zhukov et al. 2000](#); [Peter et al. 1965](#)), as well as sporadic events such as CMEs.

Observing the solar corona in white light requires perfect eclipse conditions, because the coronal brightness in this spectral

band is much fainter than the halo of diffraction produced by the Sun, typically from  $10^{-6} B_{\odot}$  to  $10^{-10} B_{\odot}$ , where  $B_{\odot}$  is the mean solar brightness ([Cox 2000](#)). By creating artificial eclipses, the first *Lyot* solar coronagraph was a breakthrough for the study of the solar corona ([Lyot 1939](#); [Dollfus 1983](#)). The development of the external occultation technique ([Evans 1948](#)) coupled with advanced stray light rejection concepts, such as toothed or multiple discs ([Newkirk & Bohlin 1965](#); [Purcell & Koomen 1962](#)), and the advent of space-borne instruments considerably improved the performance of solar coronagraphs, as described in the review paper by [Koutchmy \(1988\)](#). The solar coronagraph LASCO C2 (Large Angle Spectroscopic Coronagraph) of the Solar and Heliospheric Observatory mission can be held as a representative and successful example. This instrument combined an external occulter made of multiple discs and a *Lyot*-style solar coronagraph to achieve a sufficient rejection of residual diffracted sunlight, and managed to observe the corona in white light beyond  $1.5 R_{\odot}$ , where  $R_{\odot}$  is the radius of the Sun, with a resolution of 11.4 arcsec per pixel ([Brueckner et al. 1995](#)).

However, historically, observing the solar corona very close to the solar limb, where instrumentally scattered sunlight usually predominates, has never been successful without an eclipse of the Sun by the Moon.

The development of Formation Flying space missions will pave the way for new advanced concepts of space instrumentation by virtually enlarging instruments to unprecedented size, especially in coronagraphy. The solar coronagraph ASPIICS (Association de Satellites Pour l’Imagerie et l’Interférométrie de la Couronne Solaire) described in Lamy et al. (2010) and Renotte et al. (2015) takes advantage of the future ESA Formation Flying mission Proba-3, and is split between two spacecraft. The concept of the optical design, detailed in Galy (2015), is similar to SOHO LASCO C2. Its 1.42 m diameter external occulting disc is mounted on the Occulter Spacecraft while the *Lyot*-style solar coronagraph of 50 mm diameter aperture is carried by the Coronagraph Spacecraft positioned 144 m behind. Its theoretical angular resolution is 2.77 arcsec – with Rayleigh criterion at 550 nm. Such a large size is new in the domain of solar coronagraphy and is the main feature of ASPIICS. The hybrid coronagraph is expected to be able to observe the solar corona in white light from  $1.08 R_{\odot}$  (1036 arcsec) to  $3 R_{\odot}$  (2880 arcsec) (Lamy et al. 2010), revealing fine scale structures very close to the solar limb.

As already mentioned, solar coronagraphy is mainly constrained by the halo of diffraction from the direct sunlight, which limits any observations and drives the performance. Sensitive analysis of this particular stray light is rather complex as it includes an extended light source – the Sun – which makes such a work much more difficult than considering one single point source, as is done in the particular domain of exoplanet coronagraphy where numerous analytic studies have been done – see for instance (Cash 2006; Vanderbei et al. 2007; Flamary et al. 2014). In solar coronagraphy, only a few numerical and analytical studies of rejection performance have been published (Lenskii 1981; Aime et al. 2002; Aime 2007, 2013). We also note that the purely analytical studies of Ferrari (2007) and Ferrari et al. (2010) come with the drawback that the *Lyot* stop must equal the entrance pupil and cannot be reduced. There are also some experimental approaches, such as the works described in Fort et al. (1978), Bout et al. (2000), Venêt et al. (2010) and Landini et al. (2010). In contrast, extensive and complete analytical and numerical analysis appears nowadays mandatory, for modern advanced high-contrast instrumentation. We address this need by presenting here a general study on the performance of solar coronagraphic systems. We compute the global response of the hybrid externally occulted *Lyot* coronagraph, that we compare to the classical *Lyot* coronagraph and the external solar coronagraph. We also investigate the impact of the size of the *Lyot* mask and the stop on stray light rejection.

The paper is organized as follows. The model and the framework adopted for this study are given in Sect. 2. The mathematical wave propagation into the *Lyot*-style coronagraph is derived in Sect. 3, standing as a new computation. The comparison of the response of the different coronagraphic systems and further analysis on sizing both *Lyot* mask and stop are discussed in Sect. 4. Conclusions are given in Sect. 5.

## 2. Model of the coronagraph

### 2.1. Presentation of the model

The classical *Lyot* coronagraph is made of four key planes representing the instrument. In a previous theoretical study of this

**Table 1.** Key planes of the coronagraphic systems.

Plane	Description
O	External occulter plane
A	Aperture of the telescope
B	Focal plane of the telescope
O'	Image of plane O made by the telescope
C	Image of plane A
D	Final focal plane

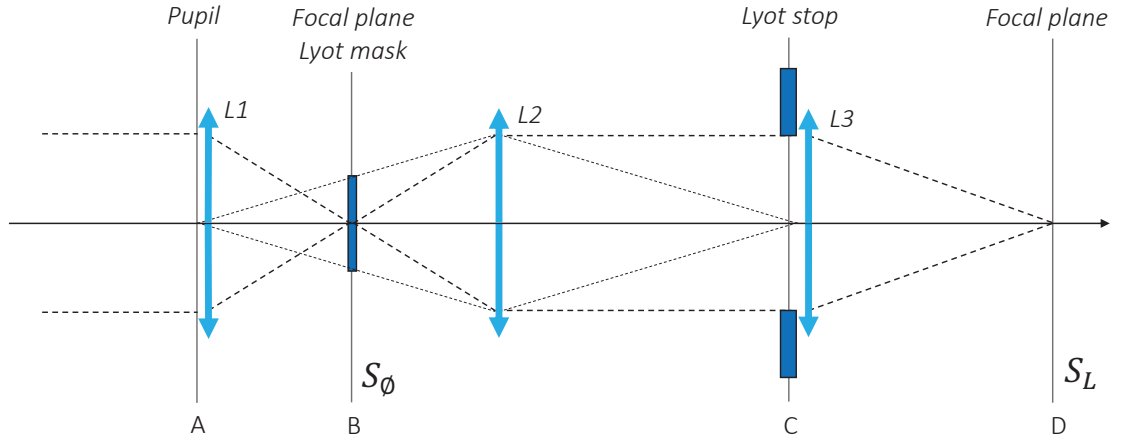
system by Aime et al. (2002), these planes are denoted as A (entrance aperture), B (focal plane), C (image of the entrance aperture) and D (final focal plane). By adding an external occulter, two additional planes must be introduced. On one hand, the external occulter is positioned in plane O at a finite distance from the entrance aperture of the telescope. On the other hand, plane O' denotes the image of the external occulter made by the telescope. It is located further behind the focal plane. In our model, we assume that the primary objective (L1) coincides with the pupil in plane A. Table 1 recalls the names and descriptions of all the planes, also illustrated in Fig. 1.

The light encounters these successive planes in the order O, A, B, O', C and D. As described previously, our work is focused on three different coronagraphic systems plus the related reference imaging system. Figure 1 presents a schematic illustration of the four systems named as follows.  $S_{\emptyset}$  denotes the raw telescope used as a reference, consisting of plane A and plane B – Fig. 1a.  $S_L$  is the classical *Lyot* coronagraph, consisting of plane A, the *Lyot* mask in plane B, and the *Lyot* stop in plane C – Fig. 1a.  $S_E$  is the externally occulted solar coronagraph, consisting of the external occulter in plane O, and ending at the focal plane B – Fig. 1b.  $S_{EL}$  denotes the hybrid externally occulted *Lyot* solar coronagraph composed of the external occulter in plane O, an internal occulter and the second objective (L2) in plane O', and the *Lyot* stop in plane C – Fig. 1b. We note that we distinguish the *Lyot* mask, denoting the occulting disc set in plane B, and the internal occulter, being in plane O' of the hybrid coronagraphic system  $S_{EL}$ . The four systems  $S_{\emptyset}$ ,  $S_L$ ,  $S_E$  and  $S_{EL}$  include the same circular entrance aperture in plane A. Table 2 summarizes the description of the four systems.

Our model is generic, and provides a methodological study on performance of such coronagraphic systems when considered as perfect. In order to have a realistic set-up, we have used the parameters of ASPIICS coronagraph (Lamy et al. 2010; Renotte et al. 2015) for the numerical computation. The external occulting disc of radius  $R = 710$  mm is located at  $z_0 = 144.348$  m before the 50 mm diameter entrance aperture. The telescope consists of a converging lens of focal length  $f = 330.385$  mm. The Sun is assumed to be at infinity. Its angular radius is  $R_{\odot} = 0.0046542$  rad as seen from the centre of the aperture, so  $\sim 960$  arcsec. The angular radius of the external occulter is  $1.0568 R_{\odot}$ , as viewed from the centre of the entrance aperture. Table 3 summarizes the numerical parameters.

The radius of the *Lyot* mask set in plane B will be given in solar units  $R_{\odot}$ , since this plane is the conjugate of the solar disc. However, the internal occulter is set in plane O' which is the conjugate image of plane O. We will thus speak in terms of units of external occulter image. A simple proportional relationship applies here to convert this particular unit system to solar units, or metric units if needed. In plane O', the image of the external occulter radius  $R$  corresponds to  $1.0568 R_{\odot}$ , so to 1.629 mm. We emphasize that using solar unit has no real meaning in plane O', since it is not conjugated with the Sun. Finally, as plane C is the

(a)



(b)

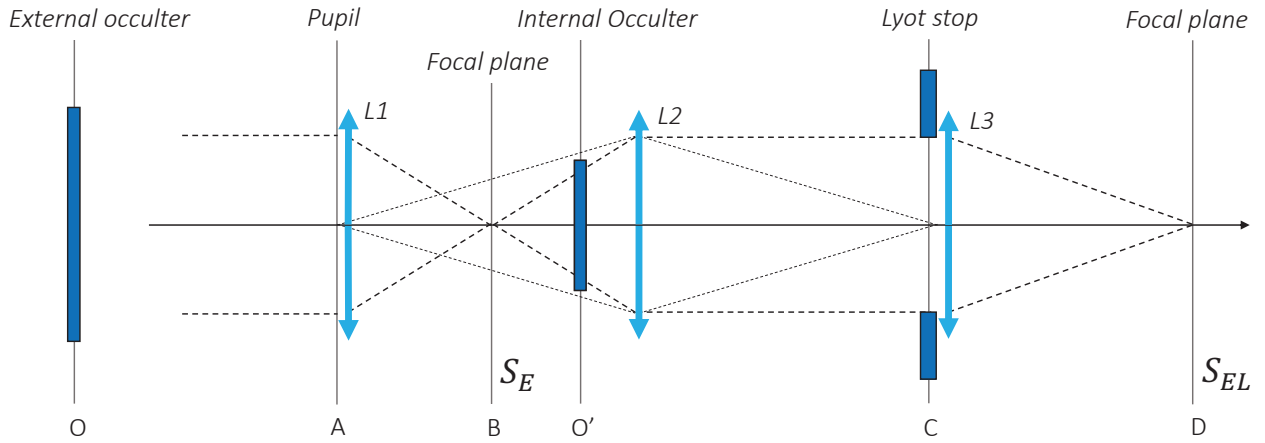


**Fig. 1.** Schematic representation of the four imaging systems. **a)** The classical *Lyot* coronagraph  $S_L$  made of planes A–D. The raw telescope  $S_0$  ends at focal plane B. **b)** The hybrid externally occulted *Lyot* solar coronagraph  $S_{EL}$  made of planes O, A, O', C and D. The externally occulted solar coronagraph  $S_E$  ends at focal plane B. Figures not to scale.

conjugate image of plane A, the dimension of the *Lyot* stop will be given in units of the image of the entrance pupil, meaning that a *Lyot* stop of 1.00 has the exact same size as the radius of the pupil in plane C, so it corresponds to  $R_p = 25$  mm.

## 2.2. Analytic and numerical framework

All the planes previously defined are assumed to be perfectly parallel and perpendicular to the optical axis, so that the geometry is axis-symmetric. We note that our model is general enough to cover transverse off-sets, but this would require further computations that are left to future works. To each plane we set a  $(r, \theta, z)$  cylindrical coordinate system. The  $z$ -axis refers to the optical axis, oriented positively towards the detection plane. The corresponding Cartesian coordinate system  $(x, y, z)$  is defined by  $x = r \cos \theta$  and  $y = r \sin \theta$ . In the remainder of the article, we will sometimes use both coordinates simultaneously, because this slight abuse of notation allows more compact and readable equations. To provide a better understanding, we will use as subscript the letter O, A, B, O', C or D referring to the corresponding plane for every quantity.

To model the perfect sharp-edged disc, the transmission in plane O is a radial gate function  $\tau(r) = 0$  if  $r > R$  and  $\tau(r) = 1$  else. The *Lyot* mask (internal occulter) in plane B (plane O') is

similarly modelled. The entrance pupil in plane A is a perfect circular aperture of radius  $R_p = 25$  mm.

Our study uses monochromatic light, here  $\lambda = 550$  nm. We have adopted a Fresnel regime to describe diffraction induced by the external occulter, as suggested by the large value of Fresnel number  $\mathcal{N}_f = R^2/\lambda z_0 = 6350$  (Born & Wolf 2006). The analytic propagation of wave front is based on paraxial Fourier optics formalism (Goodman 2005). Under this assumption, Fresnel free-space propagation of a wave front  $\Psi_0(x, y)$  over a distance  $z$  is written as convolution product. The complex amplitude  $\Psi_z(x, y)$  of the propagated wave front at distance  $z$  is

$$\begin{aligned} \Psi_z(x, y) &= \Psi_0(x, y) \otimes \frac{1}{i\lambda z} \exp\left(i\pi \frac{x^2 + y^2}{\lambda z}\right) \\ &= \frac{\varphi_z(r)}{i\lambda z} \times \mathcal{F}_{\lambda z}[\Psi_0(x, y) \times \varphi_z(r)], \end{aligned} \quad (1)$$

where  $\varphi_z(r) = \exp(i\pi r^2/\lambda z)$ , and  $r = \sqrt{x^2 + y^2}$  is the transverse radius in cylindrical coordinates.  $\mathcal{F}_{\lambda z}$  denotes the 2D Fourier transformation with spatial frequencies  $u = x/\lambda z$  and  $v = y/\lambda z$ . Equation (1) is the so-called Fourier-Fresnel transformation of the function  $\Psi_0(x, y)$ , where the phase term  $\exp(2i\pi z/\lambda)$  for the longitudinal propagation has voluntarily been omitted. Moreover, in the Fourier formalism, a converging lens of focal length  $f$  is

**Table 2.** Definition of the four imaging systems.

Name of the system		Combination of planes
$S_{\emptyset}$	Raw telescope	A + B
$S_L$	Classical <i>Lyot</i> coronagraph	A + B + C + D
$S_E$	External solar coronagraph	O + A + B
$S_{EL}$	Hybrid externally occulted <i>Lyot</i> solar coronagraph	O + A + O' + C + D

**Table 3.** Parameters for the numerical study – from ASPIICS configuration.

Parameter	Value
Wavelength	$\lambda = 550$ nm
Angular radius of the Sun	$R_{\odot} = 0.0046542$ rad $= 960$ arcsec
Distance to the Sun	$\infty$ (1 AU)
Radius of the external occulter	$R = 710$ mm
Distance plane O – plane A	$z_0 = 144.348$ m
Radius of the pupil	$R_p = 25$ mm
Focal length of the telescope	$f = 330.385$ mm

**Notes.** See text for details.

modelled by the quadratic phase factor  $\varphi_{-f}(r) = \exp(-i\pi r^2/\lambda f)$ . Propagating through a lens consists of multiplying the complex amplitude of the incoming wave front by  $\varphi_{-f}(r)$ . A well known result is the propagation to the focal plane of a lens, that is,  $z = f$  in Eq. (1). In this case, the two quadratic phase factors  $\varphi_{-f}(r)$  and  $\varphi_{+f}(r)$  cancel each other out. Consequently, the wave in the focal plane is directly proportional to the Fourier transformation of the incoming wave at its entrance, to a scale factor  $\lambda f$  and a quadratic term  $\varphi_f(r)$  that is canceled when computing the intensity.

The Sun is modelled by a collection of incoherent point sources. The global response of any system is given by the incoherent sum of their respective elementary intensities. Every point source is identified by a set of angular coordinates  $(\alpha, \beta)$  on the sky, with  $\sqrt{\alpha^2 + \beta^2} \leq R_{\odot}$ . As it will be discussed in Sect. 4.1, the number of point sources needs to be carefully fixed to meet Shannon criteria for the numerical sampling of the Sun. To provide a better understanding, we will also use as subscripts the coordinates  $(\alpha, \beta)$  to refer to a precise point source for every quantity. As the Sun is at infinity, the light coming from every point source is modelled by tilted planar wave, whose unitary complex amplitude is written as  $\Psi_{\odot, \alpha, \beta}(x, y) = \exp(-2i\pi/\lambda(\alpha x + \beta y))$ .

We use the center-to-limb variation of the Sun  $B(\alpha, \beta)$  from Hamme (1993), given in Eq. (2), to model the non-uniformity of the viewed brightness of the solar disc. This choice has been driven by the need to have a representative limb-darkening function for the specific wavelength  $\lambda = 550$  nm.

$$B(\rho) = 1 - 0.762 \left(1 - \sqrt{1 - \rho^2}\right) - 0.232 (1 - \rho^2) \log \left(\sqrt{1 - \rho^2}\right), \quad (2)$$

where  $\rho = \sqrt{\alpha^2 + \beta^2}/R_{\odot}$  is the angular radial coordinate on the solar disc, expressed in solar units.

### 2.3. Fresnel diffraction by the external occulter

Fresnel diffraction produced by a sharp-edged disc has already been described by Aime (2013, his Eq. (5)). We will briefly

recapitulate the main results of interest. The tilted planar wave front  $\Psi_{\odot, \alpha, \beta}(x, y)$  coming from the point source at  $(\alpha, \beta)$  arrives onto the occulter in plane O, and then propagates in free-space. Related complex amplitude  $\Psi_{A, \alpha, \beta}$  of the wave front arriving on plane A is thus written as a Fourier-Fresnel transformation.

$$\begin{aligned} \Psi_{A, \alpha, \beta}(x, y) &= \left[ \Psi_{\odot, \alpha, \beta}(x, y) \times \tau \right] \otimes \frac{1}{i\lambda z_0} \exp\left(i\pi \frac{x^2 + y^2}{\lambda z_0}\right) \\ &= T_{\alpha, \beta}(x, y) \times \Gamma_{\alpha, \beta} \times \Psi_{A, 0, 0}(x + \alpha z_0, y + \beta z_0), \quad (3) \end{aligned}$$

where

$$T_{\alpha, \beta}(x, y) = \exp\left(-2i\pi \frac{\alpha x + \beta y}{\lambda}\right) \quad (\text{tilt})$$

$$\Gamma_{\alpha, \beta} = \exp\left(-i\pi \frac{(\alpha^2 + \beta^2)z_0}{\lambda}\right) \quad (\text{offset})$$

$$\Psi_{A, 0, 0}(x, y) = 1 - \frac{1}{i\lambda z_0} \iint_{\eta^2 + \xi^2 \leq R^2} \exp\left(i\pi \frac{(x - \xi)^2 + (y - \eta)^2}{\lambda z_0}\right) d\xi d\eta, \quad (4)$$

with  $\xi, \eta$  the Cartesian variables for integration over the occulting disc. As a result, an off-axis point source produces the same complex amplitude as the on-axis point source –  $\Psi_{A, 0, 0}$  – but shifted of the quantity  $(z_0 \times \alpha, z_0 \times \beta)$  towards negative  $(x, y)$  directions. The constant phase term  $\Gamma_{\alpha, \beta}$  accounts for the offset of position, and the original tilt  $T_{\alpha, \beta}$  of the wave is conserved. Let us now consider the particular case of the on-axis point source. Taking advantage of the cylindrical symmetry, we naturally change for polar coordinates  $(r, \theta)$ . Equation (4) is then written as a radial Hankel transformation:

$$\Psi_{A, 0, 0}(r) = 1 - \frac{\varphi_{z_0}(r)}{i\lambda z_0} \int_0^R 2\pi\rho \exp\left(i\pi \frac{\rho^2}{\lambda z_0}\right) J_0\left(2\pi \frac{r\rho}{\lambda z_0}\right) d\rho, \quad (5)$$

where  $\rho$  is the radial variable for integration over the disc,  $r$  is the transverse radial coordinate on plane A,  $\varphi_{z_0}(r) = \exp(i\pi r^2/\lambda z_0)$  and  $J_0(r)$  is the Bessel function of the first kind. Equation (5) is the exact analytic expression of Fresnel diffraction in the particular case of the on-axis point source. The computation of the Hankel transformation  $\Psi_{A, 0, 0}(r)$  (Eq. (4)) remains a delicate operation, as described by Lemoine (1994). We chose to use NIntegrate in *Mathematica* (Wolfram 2012), since it has been proved to give sufficient numerical precision (Aime 2013). An analytic expression using the Lommel series can alternatively be used. In Fig. 2 (curve (a)), we plot Fresnel diffraction pattern  $|\Psi_{A, 0, 0}(r)|^2$ , known as the bright spot of Arago, for the 710 mm diameter disc at the distance  $z_0 = 144.348$  m, in a logarithmic scale. The distance between the first zeroes of the Arago spot is approximately  $1.53\lambda z_0/2R$ , being  $171 \mu\text{m}$  in our case. Using an analogy to Shannon's criteria, the radial sampling must be much tighter than half of this value. We voluntarily chose to over-sample at  $0.1 \mu\text{m}$ , for better 2D-interpolation. In Fig. 2, we also show the central spot in linear scale (curve (b)), whose peak intensity is 1 for  $r = 0$  as expected, and the transition zone between shadow and light (curve (c)). We note that the intensity decreases below  $10^{-4}$  for larger values of  $r$ .

## 3. Propagation through the coronagraph

The propagation of every wave front consists in a coherent process through each successive plane of the coronagraph. We successively derive  $\Psi_B$ ,  $\Psi_{O'}$ ,  $\Psi_C$ , and finally  $\Psi_D$ , for each system  $S_{\emptyset}$ ,  $S_L$ ,  $S_E$ , or  $S_{EL}$ . However, the observed response is the result

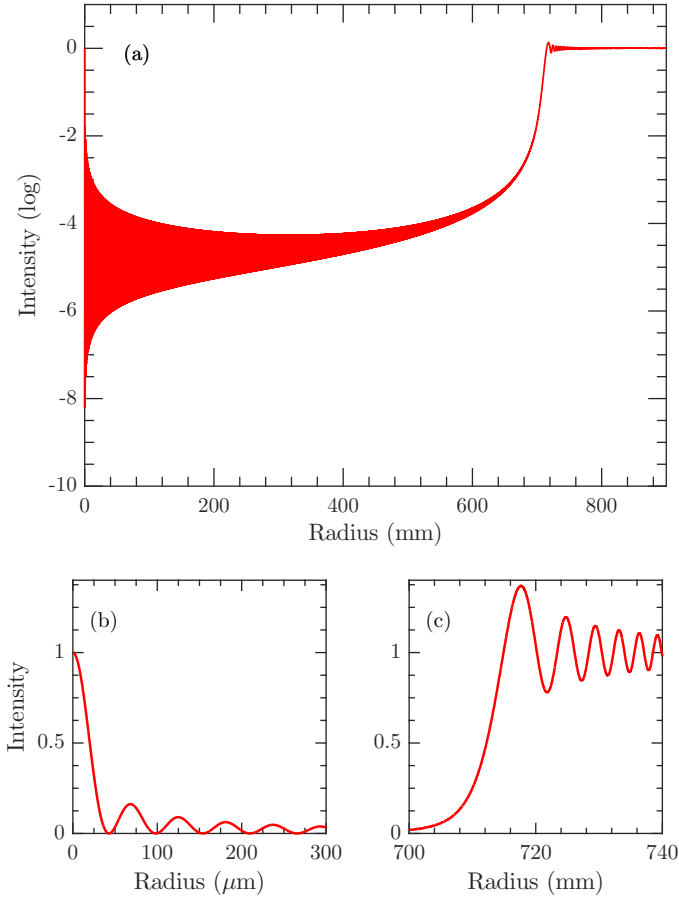


**Fig. 2.** Fresnel diffraction pattern  $|\Psi_{A,0,0}(r)|^2$  for unitary on-axis point source at infinity, for the 710 mm radius occulting disc at  $z_0 = 144.348$  m. **a)** Full range, in logarithmic scale. **b)** Zoom in the Arago bright spot in the central region  $[0, 500 \mu\text{m}]$ , in linear scale. **c)** Transition region between shadow and light around 710 mm, in linear scale.

of the incoherent summation of every elementary intensity. So, let us consider one point source located at  $(\alpha, \beta)$  on the solar disc. In this section, we will voluntarily omit the subscripts  $(\alpha, \beta)$  for a better readability, and we will preferably use polar coordinates  $(r, \theta)$  rather than the Cartesian coordinates  $(x, y)$ .

### 3.1. Classical *Lyot* coronagraph

As already described, the classical *Lyot* coronagraph  $S_L$  is modelled by planes A, B, C and D (Aime et al. 2002), and does not include the external occulter. At the entrance aperture,  $\Psi_A$  corresponds then to a simple tilted planar wave front. Here, the coronagraph acts as a mere imaging system, adding the *Lyot* mask in the focal plane. Using the approach of Fourier formalism described in Sect. 2.2, the propagation process through the whole instrument consists in scaled Fourier transformations between each of the successive planes, that is, from A to B, from B to C and from C to D. The images are of different sizes, depending on the lenses used for imaging, but these variations in size do not affect the result. In terms of Fourier analysis, the *Lyot* mask in B behaves as a high-pass filter and the *Lyot* stop in C behaves as a low-pass filter. It is the conjugate effect of these two masks that makes the *Lyot* coronagraph efficient for the rejection of the direct sunlight where we want to observe the corona.

We name  $\mathcal{P}(r)$ ,  $\mathcal{M}(r)$  and  $\mathcal{L}(r)$  the radial transmission functions of the entrance pupil in A, the *Lyot* mask in B and the *Lyot*

stop in C respectively. The wave front  $\Psi_B$  in the focal plane of the objective L1 results of a Fourier transformation, as described in Sect. 2.2.

$$\Psi_B(r, \theta) = \frac{\varphi_f(r)}{i\lambda f} \times \tilde{\Psi}_B(r, \theta), \quad (6)$$

where  $\tilde{\Psi}_B(r, \theta) = \mathcal{F}_{\lambda f} [\Psi_A(r, \theta) \times \mathcal{P}(r)]$ . Therefore, the intensity in plane B is merely proportional to the Fourier transformation of  $\Psi_A(r, \theta) \times \mathcal{P}(r)$ . The wave front in plane B encounters the *Lyot* mask  $\mathcal{M}(r)$  and the second objective L2 of focal  $f_2$ . Plane C is the image of the entrance aperture that is located at a distance  $d = f \times f_2 / (f - f_2)$  from plane B, as given by the relation of conjugation for lens. Writing a Fourier-Fresnel transformation of  $\Psi_B$  over the distance  $d$ , the three quadratic phase factors  $\varphi_f(r)$ ,  $\varphi_{-f_2}(r)$ , and  $\varphi_d(r)$  cancel each other out.

$$\begin{aligned} \Psi_C(r, \theta) &= \frac{\varphi_d(r)}{i\lambda d} \times \mathcal{F}_{\lambda d} [\Psi_B(r, \theta) \times \mathcal{M}(r) \times \varphi_{-f_2}(r) \times \varphi_d(r)] \\ &= \frac{-\varphi_d(r)}{\lambda^2 f d} \times \tilde{\Psi}_C(r, \theta), \end{aligned} \quad (7)$$

where  $\tilde{\Psi}_C(r, \theta) = \mathcal{F}_{\lambda d} [\tilde{\Psi}_B(r, \theta) \times \mathcal{M}(r)]$ . Again, the intensity in plane C is proportional to the Fourier transformation of  $\tilde{\Psi}_B(r, \theta) \times \mathcal{M}(r)$  (Aime et al. 2002). Based on the same principle, the wave front in plane D is obtained by performing a Fourier transformation of  $\tilde{\Psi}_C(r, \theta) \times \mathcal{L}(r)$ , corresponding to the image on the focal plane of the whole imaging system.

$$\Psi_D(r, \theta) = \frac{\varphi_f(r)}{i\lambda f} \times \mathcal{F}_{\lambda f} [\tilde{\Psi}_C(r, \theta) \times \mathcal{L}(r)]. \quad (8)$$

The wave propagation for the reference telescope  $S_\emptyset$  is limited to the first propagation to plane B as described in Eq. (6). We also applied this analytic formulation to the external solar coronagraph  $S_E$  by considering Fresnel diffraction for the complex amplitude  $\Psi_A$  at the entrance aperture, given by Eq. (3).

### 3.2. Hybrid externally occulted *Lyot* solar coronagraph

Let us now consider the hybrid coronagraph  $S_{EL}$ . This system varies from the classical *Lyot* coronagraph  $S_L$ , since it has the internal occulter in plane O'. Plane B has no more actual interest in this particular case and shall be skipped. Moreover,  $\Psi_A$  consists now of Fresnel diffracted wave front as given in Eq. (3), because of the external occulter in plane O. We directly write the Fourier-Fresnel propagation over the distance  $z_1 = z_0 f / (z_0 - f)$  between planes A and O'. The wave front  $\Psi_{O'}$  in plane O' is then expressed as

$$\begin{aligned} \Psi_{O'}(r, \theta) &= \frac{\varphi_{z_1}(r)}{i\lambda z_1} \times \mathcal{F}_{\lambda z_1} [\Psi_A(r, \theta) \times \mathcal{P}(r) \times \varphi_{-f}(r) \times \varphi_{z_1}(r)] \\ \Psi_{O'}(r, \theta) &= \frac{\varphi_{z_1}(r)}{i\lambda z_1} \times \tilde{\Psi}_{O'}(r, \theta), \end{aligned} \quad (9)$$

where  $\tilde{\Psi}_{O'}(r, \theta) = \mathcal{F}_{\lambda z_1} [\Psi_A(r, \theta) \times \mathcal{P}(r) \times \varphi_{-z_0}(r)]$ . The main difference between  $\tilde{\Psi}_B$  in Eq. (6) and  $\tilde{\Psi}_{O'}$  in Eq. (9) is the quadratic phase factor  $\varphi_{-z_0}(r) = \exp(-i\pi r^2 / \lambda z_0)$ . It can be interpreted as a virtual converging lens of focal length  $z_0$  which rejects the external occulter at infinity. Consequently, the image of plane O made by the primary objective is now moved into the focal plane, and so it is computed as a simple Fourier transformation, as previously. This reasoning makes the computations much more convenient than first considering the wave in plane B and then

propagating it to O' using Fresnel propagation over the distance  $f^2/(z_0 - f)$ .

Then, the wave front in plane O' encounters the internal occulter  $\mathcal{M}(r)$  and the second objective L2. Here, we can directly apply Eq. (7) to derive the complex amplitude of the wave front in plane C, where the distance  $d$  becomes now to  $d = z_1 \times f_2 / (z_1 - f_2)$ . However, the quadratic phase factor  $\varphi_{-z_0}(r)$  remains. Since we want to obtain in plane C the exact image of the pupil, we have to get rid of this unwanted factor. This is simply obtained by multiplying the complex amplitude in plane C by  $\varphi_{+z_0}(r)$ , which corresponds to a diverging lens of focal  $z_0$  that compensates the first virtual converging lens.

$$\Psi_C(r, \theta) = \frac{-\varphi_d(r)}{\lambda^2 z_1 d} \times \widetilde{\Psi}_C(r, \theta) \times \varphi_{+z_0}(r), \quad (10)$$

where  $\widetilde{\Psi}_C(r, \theta) = \mathcal{F}_{\lambda d_2} [\widetilde{\Psi}_{O'}(r, \theta) \times \mathcal{M}(r)]$ . Finally, the wave front in plane D is given by Eq. (8).

### 3.3. Observed intensities

The total intensity  $I_{\mathcal{K}}$  on plane  $\mathcal{K} \in \{A, B, O', C, D\}$  is the incoherent sum of the elementary intensities due to every points source describing the whole solar disc. From here, the complex amplitude  $\Psi_{\mathcal{K}, \alpha, \beta}(r, \theta)$  will be written as a function of four variables  $\Psi_{\mathcal{K}}(\alpha, \beta, r, \theta)$ , to clarify the integration process. Taking into account the center-to-limb darkening function  $B(\alpha, \beta)$ , the integrated intensity due to the whole solar disc is

$$I_{\mathcal{K}}(r, \theta) = \iint B(\alpha, \beta) \times |\Psi_{\mathcal{K}}(\alpha, \beta, r, \theta)|^2 d\alpha d\beta, \quad (11)$$

where  $\mathcal{K} \in \{A, B, O', C, D\}$ . This Fredholm integral of the first kind cannot be computed as a mere convolution since  $\Psi_{\mathcal{K}}(\alpha, \beta, r, \theta)$  is not shift invariant with respect to  $(\alpha, \beta)$ . So a 2D numerical summation must be performed, and the integral in Eq. (11) shall be transformed into a finite sum, using discrete values  $\alpha_k$  and  $\beta_l$  for  $\alpha$  and  $\beta$ . We emphasize that for each  $\alpha_k$  and  $\beta_l$  we obtain a elementary 2D image. The required number of sampling points on the solar disc, that is,  $k$  and  $l$ , can be derived using Shannon criteria of the interpolation formula. The sampling must be tighter than  $0.5\lambda/D_p$  radian, with  $D_p = 2R_p$  the diameter of the entrance pupil. This corresponds to an upper limit of 1.13 arcsec in our case, being a minimum of 1692 points in a solar diameter, or about 2.25 millions points on the whole solar disc. For the general Fredholm integral, the derivation of the required number of samples is not so straightforward, but the result is the same due to the inherent nature of band limited images. The computation of the final observed intensity in plane D therefore requires three times as much 2D Fast Fourier transformations as the number of sampling points on the solar disc – 6.75 million.

At this stage, we can actually take advantage of the axis-symmetry of the system. We remind the reader that it assumes that the Sun and every remarkable planes are parallel and aligned to the optical axis. In Eq. (11), we now replace solar angular coordinates  $(\alpha, \beta)$  by  $(\rho, \theta_s)$ , with  $\alpha = \rho \cos \theta_s$  and  $\beta = \rho \sin \theta_s$ , meaning having  $\rho \in [0, R_\odot]$  and  $\theta_s \in [0, 2\pi]$ . The assumed symmetry makes the 2D image of one point source  $|\Psi_{\mathcal{K}}(\rho, \theta_s, r, \theta)|^2$  in plane  $\mathcal{K}$  rotate identically with respect to the point source on the solar disc, that is,  $\theta_s$ . In other words, it only depends on the relative angular difference  $\phi = \theta - \theta_s$ . As a result, integrating over the solar polar angle  $\theta_s$  is equivalent to circularly integrating on the 2D image plane, so over  $\theta$ . Moreover, the solar brightness is a radial function, so  $B(\alpha, \beta) = B(\rho)$ . By substituting  $\theta$  by  $\phi$ ,

the integrated intensity given in Eq. (11) becomes the following radial function

$$I_{\mathcal{K}}(r) = \int_0^{2\pi} \left[ \int_0^{R_\odot} B(\rho) \times |\Psi_{\mathcal{K}}(\rho, \theta_s, r, \phi + \theta_s)|^2 \rho d\rho \right] d\phi. \quad (12)$$

From a numerical point of view, it is much more convenient to compute this last integral than the rough full two-dimension summation. In Eq. (12),  $\theta_s$  can arbitrarily be fixed to 0, since the integration is performed over  $2\pi$ , so we choose  $\alpha = \rho$  and  $\beta = 0$ . This means that we only need to propagate the wave fronts coming from the point sources of one elementary radius of the Sun. The integration is thus performed as a weighted numerical summation of two-dimension images, using discrete values  $\rho_k$  to sample the solar radius, using the sampling requirement defined above, followed by a circular average of the result.

## 4. Analysis and discussion

### 4.1. Numerical implementation

We now present the results of the complete computation of the observed intensities  $I_{\mathcal{K}}(r)$  on each plane  $\mathcal{K} \in \{A, B, O', C, D\}$ , accordingly for each configuration  $S_\emptyset, S_L, S_E$  and  $S_{EL}$ . Using the complex amplitude  $\Psi_A$  computed with *Mathematica*, the wave front is linearly interpolated and the propagation is performed with MATLAB 2D Fast Fourier transformation combined with the re-centering routine `fftshift` when necessary. In addition to this paper, we provide a dedicated MATLAB/OCTAVE toolbox, whose content will be continuously updated, for the sake of reproducible research<sup>1</sup>.

A difficult and sensitive parameter in this numerical study is the choice of the sampling in each plane. Indeed, as discussed in Soummer et al. (2007), in successive planes (A to B or A to O', B to C or O' to C, and C to D), the sampling requirements are opposite. This problem is known as the two-fold sampling requirement. The point of view which has been adopted in the present work is somewhat empirical. We imposed the same number of points in the occulter image in plane O' and in the telescope aperture in plane A. We note that this a priori is sensible since it provide a similar resolution in all planes, but other sampling strategies might be of interest. The telescope aperture is padded inside an array of  $N \times N$  points, and  $n_p < N$  points are used in the radius  $R_p$  of the aperture. The spatial sampling in plane A is thus  $s_A = R_p/n_p$ , for a total spatial field  $F_A = N \times R_p/n_p$ . Due to the properties of Fourier spatial frequencies, the field  $F_A$  in plane A produces a sampling  $s_{O'} = \lambda d/F_A$  in plane O', where  $d = z_0 f / (z_0 - f)$  is the distance between plane A and plane O'. Moreover, the size of the image of the external occulter radius is  $R \times d/z_0$ . Therefore, the corresponding number of points  $n_r$  in plane O' is  $n_r = R d / z_0 s_{O'}$ . By imposing  $n_r = n_p$ , we obtain:

$$n_r = \sqrt{\frac{R \times R_p \times N}{z_0 \times \lambda}} \sim 14.9525 \sqrt{N}. \quad (13)$$

For numerical reasons,  $N$  should preferably be a power of two, and at least 4096 points are required for a correct sampling of the image to respect Shannon criterion. Of course, the larger  $N$  the better the result due to zero-padding effect, being a compromise between computation time and precision.

The results of computation reported in this paper have been made using a machine with two 14 core Intel Xeon processors and 512 GB of RAM, using  $N = 2^{13} = 8192$ , giving  $n_p = 1353$ ,

<sup>1</sup> This package can be found at the following link: <https://github.com/rrougeot/FourierOptics>

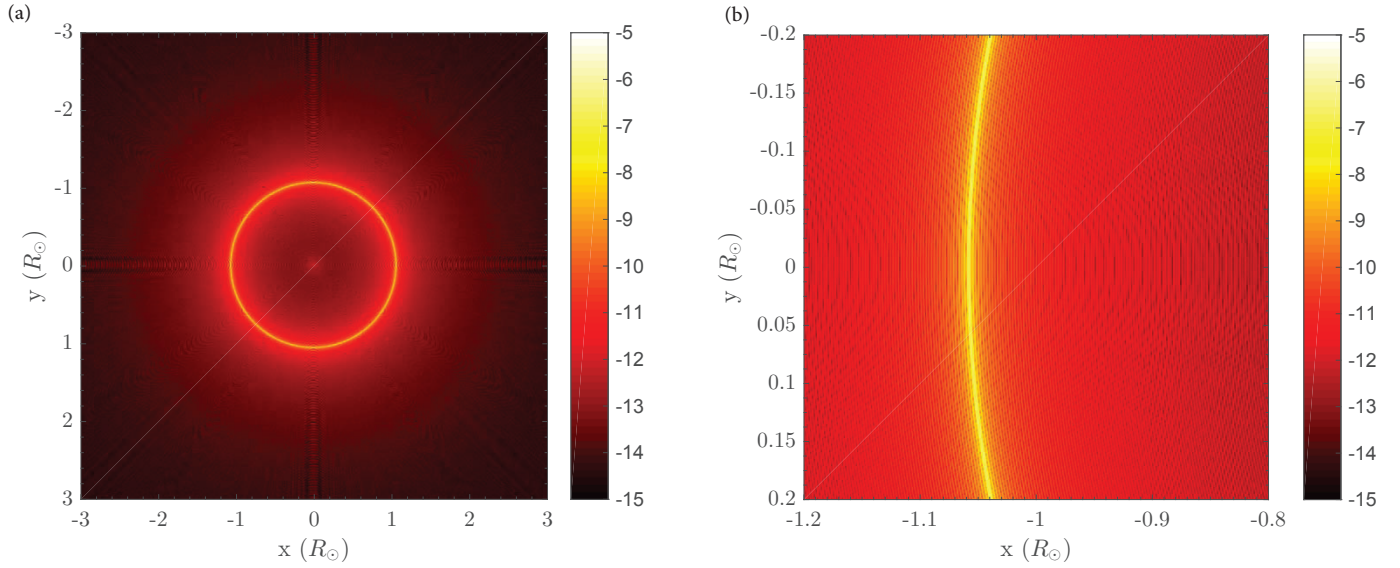


**Fig. 3.** Two-dimension observed intensity in plane  $O'$  of diffracted wave front originating from the on-axis point source at the center of the Sun, in logarithmic scale. **a)** Full field. **b)** Zoomed in region of interest around  $1.08 R_{\odot}$ .

which corresponds to a sampling of  $18.5 \mu\text{m}$  and a spatial field of  $15.6 \text{ cm}$  in plane A. We chose to over-sample the solar radius by setting 1000 point sources rather than 846. Each step in the numerical computation has been verified in particular with point sources. We used a *Lyot* mask or internal occulter of  $1.065 R_{\odot}$  radius and a *Lyot* stop sizing 0.99 times the entrance aperture image, to illustrate the numerical study. Despite the fact that the size of the *Lyot* stop is only scaled to the size of the entrance aperture, we warn the reader that the results strongly depend on the value of  $R_p$ .

#### 4.2. Impulse response in the *Lyot* coronagraph

We investigate the impulse response originating from one point source in both plane B and  $O'$ , while adding the external occulter in plane O. We first analyzed the on-axis point source. In this case, the response is symmetric, and the image is a bright circle which perfectly fits the image of the external occulter edge. In plane  $O'$ , this circle is very thin, as illustrated in Fig. 3. The intensity is focused as if the edge of the external occulter emits light as a real object. The response in plane B consists in a larger blurred circle, as expected. Second, we analyzed the response from the off-axis point source at  $\alpha = 768 \text{ arcsec}$ , i.e.  $0.8 R_{\odot}$ . Figure 4 shows the two-dimension intensities in both plane B (plots (a) and (b)) and  $O'$  (plots (c) and (d)). The shift of the Arago spot produces strongly asymmetric light pattern, while the on-axis case was perfectly symmetric. The sharpness and the fine scale structure of the diffraction features, as shown in plots (b) and (d) in Fig. 4, for plane B and  $O'$  respectively, prove the need of a very high sampling on both planes. A very dominant point is that the light pattern in plane B tends to be spread perpendicularly to the local edge of the image of the external occulter. On the contrary, plane  $O'$  shows a diffracted light pattern fitting locally the image of the external occulter.

#### 4.3. Response of the different coronagraphic systems

##### 4.3.1. Intensity in plane A

The rejection from the external occulter can first be assessed by computing the intensity  $I_A(r)$  at the entrance aperture of the

telescope. In Fig. 5, we plot the penumbra profile of diffracted light and its corresponding geometrical umbra profile. The horizontal axis represents the radial coordinate in mm, starting at the center of the umbra cone. The occulter disc is  $1.0568$  larger than the solar stenope image, which corresponds to a geometrical umbra of  $R - z_0 \tan R_{\odot} = 38 \text{ mm}$  radius, and the intensity is equal to the full solar irradiance beyond  $R + z_0 \tan R_{\odot} = 1382 \text{ mm}$ . Because of diffraction, the scattered light remains at a level of  $10^{-4} B_{\odot}$  at the center of the umbra cone, as a flat plateau. The external occultation has therefore reduced direct sunlight by four orders of magnitude at the entrance aperture, which is a first significant advantage for both externally occulted systems  $S_E$  and  $S_{EL}$ . Here, apodization techniques (Aime 2013) or more complex shapes of occulter (Bout et al. 2000) may improve the performance. In Appendix A, variations of the distance  $z_0$  are investigated, and we provide a plot illustrating different penumbra profile.

##### 4.3.2. Intensity in plane B

Figure 6 shows the radial intensities  $I_B(r)$  in plane B, limited to  $3.2 R_{\odot}$ , in logarithmic scale. Here, the image of the Sun (blue curve) is perfectly focused, and is used as a reference for normalization. This consists of the global response of the raw telescope  $S_{\emptyset}$ . The center-to-limb variation is apparent as a slight decrease in the range  $0-1 R_{\odot}$ . Sunlight falls abruptly to  $10^{-3} B_{\odot}$  at  $1 R_{\odot}$ , then extends as a large tail of residual light brighter than  $10^{-5} B_{\odot}$ . This comes from the summation of the Airy rings at large radius. The diffracted light pattern produced by the external occulter consists of a bell-like curve out-of-focus, as expected, since the focal plane is not the conjugate image plane of the external occulter. The width of this peak is function of the size of the entrance aperture, like the Airy radius. We note that the peak is not symmetric, and reaches a maximum of  $10^{-3} B_{\odot}$  around  $1.05 R_{\odot}$ . This last curve models the response of the externally occulted solar coronagraph  $S_E$ .

##### 4.3.3. Intensity in plane $O'$

Similarly, Figure 7 shows the radial intensities  $I_{O'}(r)$  in plane  $O'$  in logarithmic scale, using the same scaled axis as Fig. 6 for a

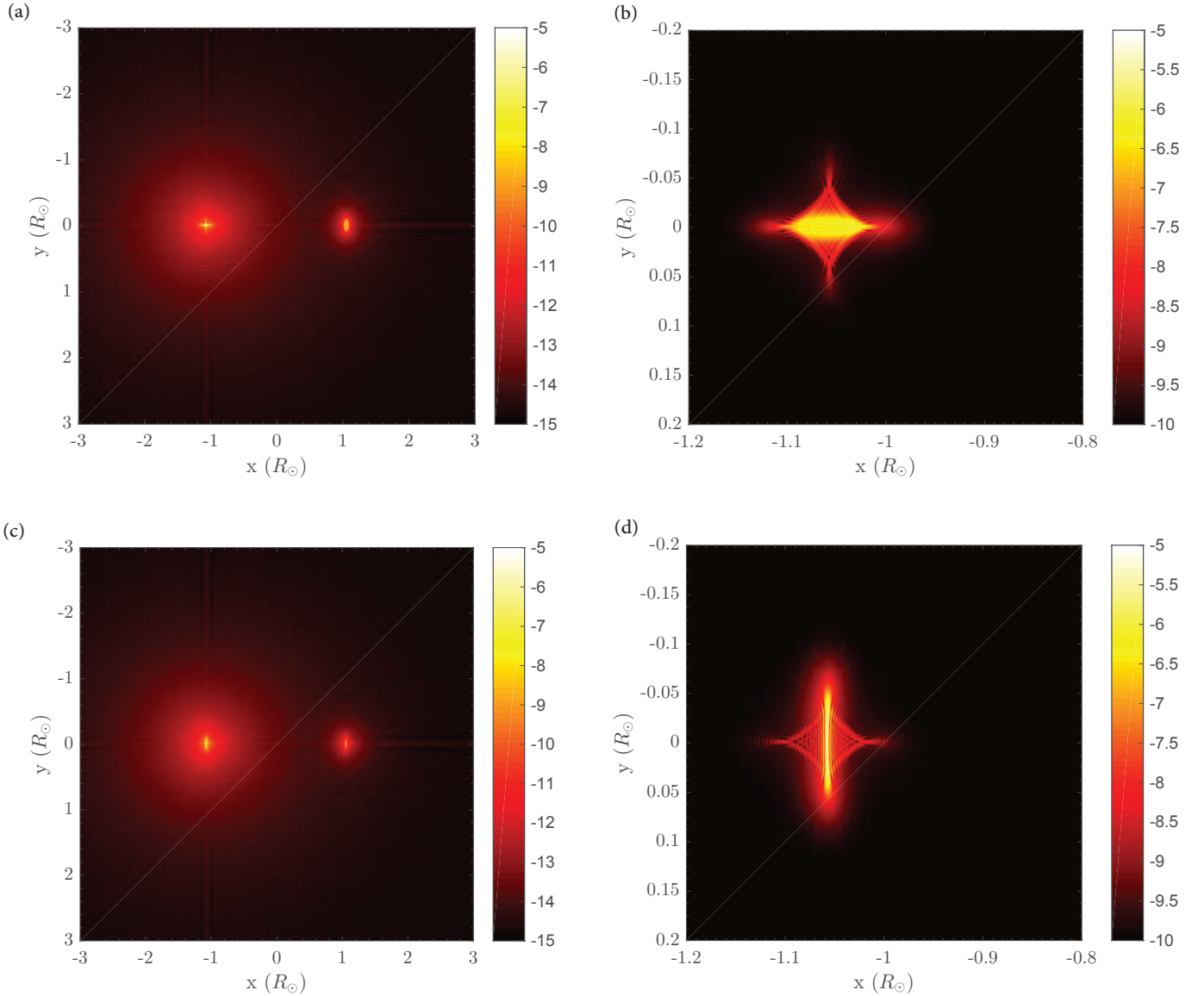


**Fig. 4.** Two-dimension observed intensities of diffracted wave front originating from the off-axis point source at  $\alpha = 768$  arcsec, in logarithmic scale. **a)**  $I_B(x, y)$  in plane B. **b)**  $I_B(x, y)$  enlarged in region of interest around  $1.08 R_\odot$ . **c)**  $I_{O'}(x, y)$  in plane  $O'$ . **d)**  $I_{O'}(x, y)$  zoomed in region of interest around  $1.08 R_\odot$ .

purpose of comparison. We remind the reader that using solar units here has no real meaning, since plane  $O'$  is not conjugated with the Sun as discussed in Sect. 2.1. The image of the Sun is very similar to the one in the focal plane – Fig. 6, but is slightly out-of-focus here, as it is at  $d - f = 0.758$  mm ahead. The drop to  $10^{-3} B_\odot$  is consequently smoother. The large tail of residual light is still present. The diffracted light by the external occulter is now focused in a very narrow peak of  $10^{-2} B_\odot$  amplitude, located at the exact angular position of the edge of the external occulter image, i.e.  $1.0568 R_\odot$  or  $1.629$  mm. This feature is expected because plane  $O'$  is the conjugate image plane of the external occulter.

#### 4.3.4. Residual light

Before inspecting the observed intensity in plane C and plane D, it is interesting to look at the integrated residual light on both planes B and  $O'$ . In the classical *Lyot* coronagraph  $S_L$ , the *Lyot* mask is set in the focal plane and blocks the direct focused sunlight (Fig. 6). A relatively large amount of residual light yet

propagates further inside the instrument. In the case of the hybrid externally occulted *Lyot* coronagraph  $S_{EL}$ , the internal occulter blocks the diffracted light fringe (Fig. 7), and its dimension governs the rejection. For comparison, we looked at the integrated residual light denoted as

$$L(r) = \int_0^{2\pi} d\theta \int_r^{\bar{r}} I_{\mathcal{K}}(r) r dr, \quad (14)$$

where  $\mathcal{K} \in B, O'$ , and with the numerical upper limit  $\bar{r} = 3.2 R_\odot$ . We analyzed the three following cases:

- $L_{\emptyset, B}(r)$  the residual light in plane  $\mathcal{K} = B$  without the external occulter;
- $L_{E, B}(r)$  the residual light in plane  $\mathcal{K} = B$  including the external occulter;
- $L_{E, O'}(r)$  the residual light in plane  $\mathcal{K} = O'$  including the external occulter.

We superimposed the three normalized integrated residual light curves  $L_{\emptyset, B}(r)$ ,  $L_{E, B}(r)$ , and  $L_{E, O'}(r)$  onto Fig. 8. The curve

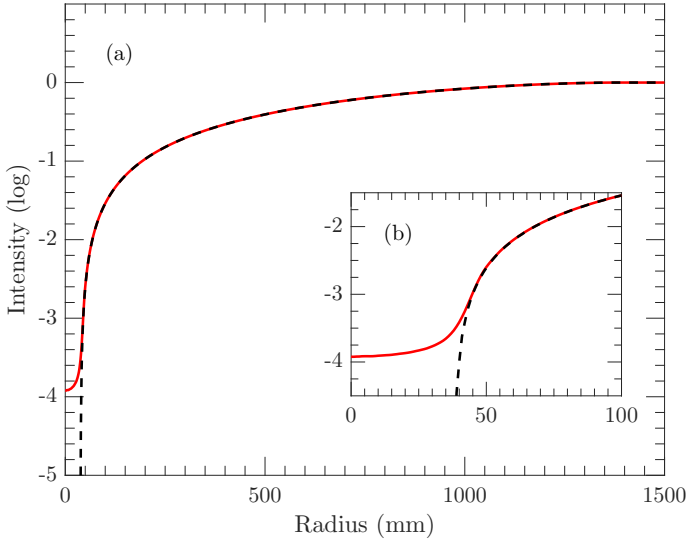


**Fig. 5.** Intensity  $I_A(r)$  in plane A, in logarithmic scale. The intensity is normalized to the mean solar brightness. Red: radial profile of diffracted light produced by the external occulter. Black dashed: related geometrical profile. **a)** Penumbra profile in full range. **b)** Enlargement in [0 mm; 100 mm] corresponding to the umbra region.

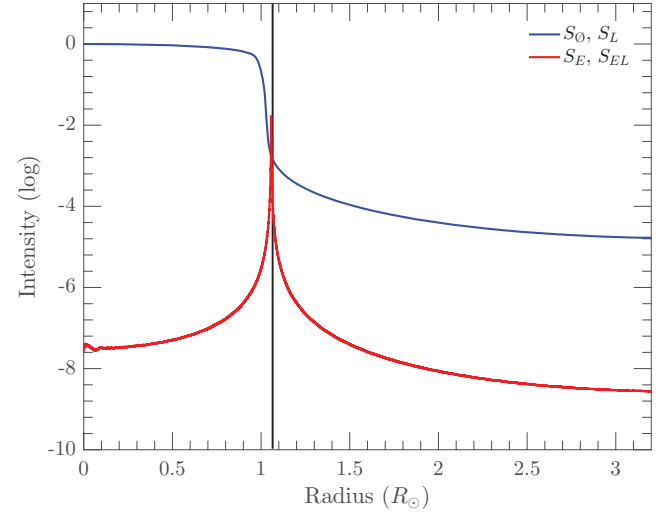


**Fig. 7.** Observed intensities  $I_{O'}(r)$  in plane  $O'$ , in logarithmic scale. The transverse radius is given in solar units. The intensities are normalized to the mean solar brightness. Blue: raw image of the Sun in plane  $O'$ . Red: diffracted sunlight by the external occulter. Vertical line:  $1.065 R_\odot$  radius internal occulter.

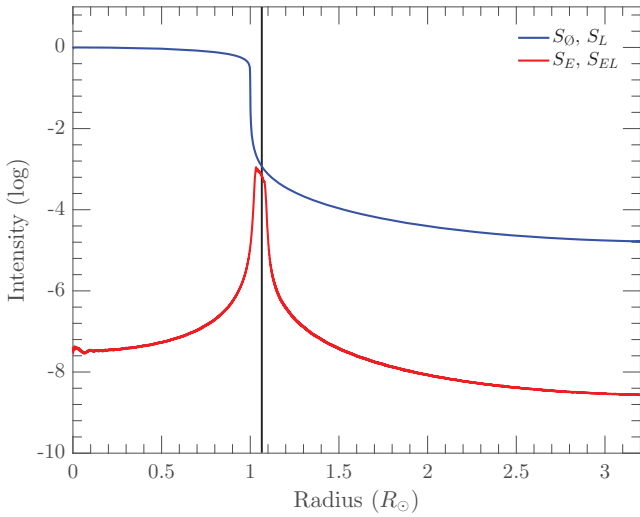


**Fig. 6.** Observed intensities  $I_B(r)$  in plane B, in logarithmic scale. The transverse radius is given in solar units. The intensities are normalized to the mean solar brightness. Blue: raw image of the Sun in plane B. Red: diffracted sunlight by the external occulter. Vertical line:  $1.065 R_\odot$  radius *Lyot* mask.

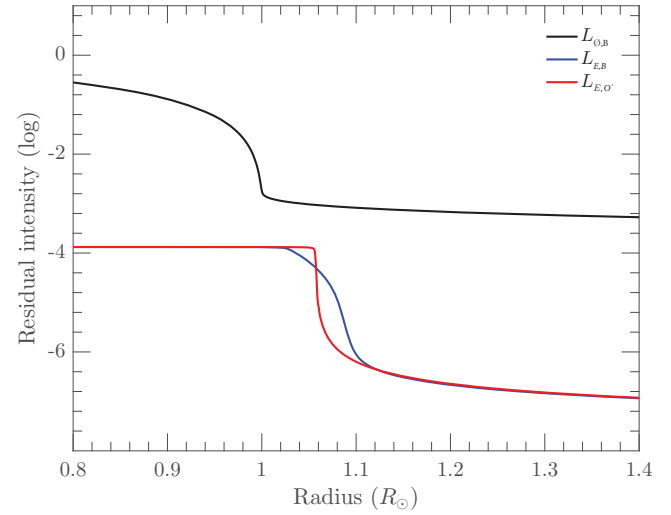


**Fig. 8.** Integrated residual light  $L(r)$ , as given in Eq. (14), in logarithmic scale, and normalized. Enlargement in the range  $[0.8 R_\odot, 1.4 R_\odot]$ . Black:  $L_{O,B}$ . Blue:  $L_{E,B}$ . Red:  $L_{E,O'}$ .

$L_{O,B}(r)$  is used for normalization and provides the amount of residual light that is not blocked for a given *Lyot* mask of radius  $r$  in the classical *Lyot* coronagraph  $S_L$ . When adding the external occulter, the residual light is already reduced by a factor  $10^{-4} \sim I_A(0)$ , and there is an appreciable difference between planes B and  $O'$ . The integrated residual light decreases relatively slowly in plane B, from  $10^{-4} B_\odot$  at  $r = 1.02 R_\odot$  and loosing two orders of magnitude over  $0.1 R_\odot$ . In plane  $O'$ , the decrease is very abrupt, from  $10^{-4} B_\odot$  at  $r = 1.06 R_\odot$  and loosing two orders of magnitude over  $0.06 R_\odot$ . As a conclusion, this shows that the internal occulter will filter out a larger amount of diffracted sunlight by being set in plane  $O'$  rather than plane B, for a given size. We provide a definitive confirmation of this last statement in Appendix B, by looking at the final response in plane D.

#### 4.3.5. Intensities in plane C

In Fig. 9 we present the radial intensities  $I_C(r)$  in plane C in logarithmic scale. The transverse radius is given in units of entrance aperture image, meaning that a radius of one corresponds to the image of  $R_p = 25$  mm. A  $1.065 R_\odot$  *Lyot* mask and an internal occulter of equivalent angular size have been used here, for the systems  $S_L$  and  $S_{EL}$  respectively. We normalized the intensities using the exact image of the entrance pupil. The classical *Lyot* coronagraph  $S_L$  shows a narrow peak at  $r = 1$ , being the exact position of the image of the pupil edge. This  $10^{-1} B_\odot$  fringe is produced by the diffraction of sunlight by the entrance aperture. A similar feature is observed in the case of the hybrid externally occulted *Lyot* coronagraph  $S_{EL}$ . The diffraction fringe is however much less bright, reaching about  $10^{-4} B_\odot$ , due to the external occultation beforehand. The role of the *Lyot* stop is to block this diffracted light peak.

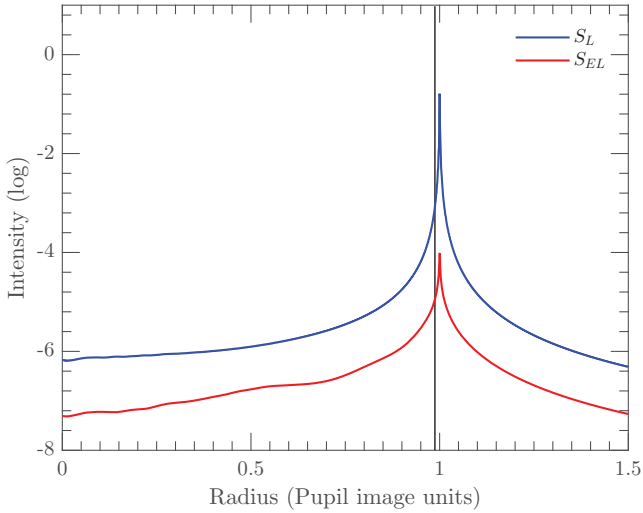


**Fig. 9.** Observed intensities  $I_C(r)$  in plane C, in logarithmic scale. The transverse radius is given in unit of image of the entrance pupil. The intensities are normalized to the mean solar brightness. Blue: system  $S_L$ . Red: system  $S_{EL}$ . Vertical line: *Lyot* stop of 0.99 times the image of the entrance pupil.

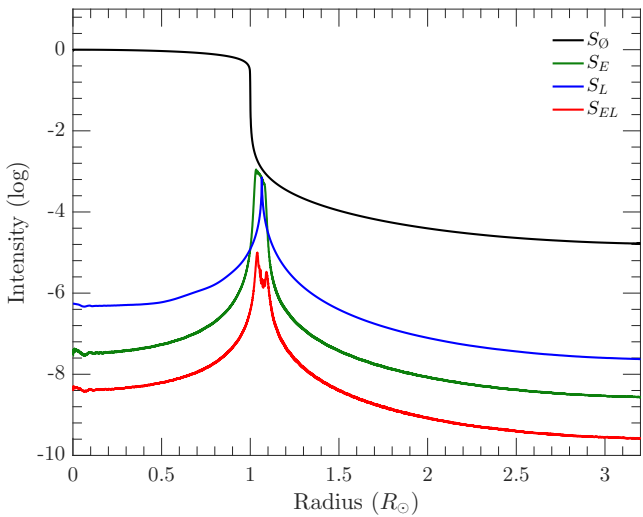


**Fig. 10.** Observed intensities as final response in the focal plane, in logarithmic scale. The transverse radius is given in solar units. The intensities are normalized to the mean solar brightness. Black: system  $S_0$  given by  $I_B(r)$  in plane B. Blue: system  $S_L$  given by  $I_D(r)$  in plane D. Black: system  $S_E$  given by  $I_B(r)$  in plane B. Red: system  $S_{EL}$  given by  $I_D(r)$  in plane D.

#### 4.3.6. Intensities in plane D

Finally, in Fig. 10 we give the final response of the four imaging systems, in logarithmic scale, using the same occulting masks of  $1.065 R_\odot$  in planes B and  $O'$ , and a *Lyot* stop of 0.99 times the image of the pupil  $-24.75$  mm in 1:1-scale. We superimposed the four observed intensities, meaning  $I_B(r)$  for the reference telescope  $S_0$  and for the external coronagraph  $S_E$ , and  $I_D(r)$  for the classical *Lyot* coronagraph  $S_L$  and for the hybrid coronagraphic system  $S_{EL}$ . The reference image of the Sun in plane B is used as a reference for normalization. Both systems  $S_L$  and  $S_E$  show a relatively bright ( $10^{-3} B_\odot$ ) diffraction fringe located around  $1.065 R_\odot$ , while the hybrid coronagraphic system  $S_{EL}$  already rejects sunlight below  $10^{-5} B_\odot$ . Outside  $1.5 R_\odot$ , the three systems  $S_L$ ,  $S_E$  and  $S_{EL}$  reject below  $10^{-6} B_\odot$ ,  $10^{-7} B_\odot$  and

$10^{-8} B_\odot$  respectively. As for now, this analysis has proved the efficiency of combining external occultation with an internally occulted *Lyot*-style coronagraph, compared to the classical *Lyot* coronagraph, with a gain of at least two orders of magnitude.

#### 4.4. Sizing the internal occulter and the *Lyot* stop

We now consider the hybrid externally occulted *Lyot* coronagraph  $S_{EL}$  only. We investigated the impact of sizing the internal occulter on the observed intensity in plane D, while keeping the external occultation ratio  $R/z_0$  constant. We looked at radii of 1.005, 1.01, 1.02, 1.03 and 1.04 times the external occulter image. They respectively correspond, in angular units (metric units), to  $1.0621 R_\odot$  (1.637 mm),  $1.0674 R_\odot$  (1.645 mm),  $1.0779 R_\odot$  (1.662 mm),  $1.0885 R_\odot$  (1.678 mm) and  $1.0991 R_\odot$  (1.694 mm). We superimpose onto Fig. 11 the radial cuts of intensities  $I_D(r)$ , in logarithmic scale, using a *Lyot* stop of 0.99 (plot (a)) and one of 0.96 (plot (b)) entrance pupil image. The plot is given in the range  $0.5$ – $2 R_\odot$  to zoom in the diffraction fringe area.

In a similar way, we analyzed the effect of sizing the *Lyot* stop, keeping a fixed internal occulter. In Fig. 12, we compare the radial cuts of final intensities  $I_D(r)$ , in logarithmic scale, using an internal occulter of 1.01 (plot (a)) and one of 1.03 external occulter image (plot (b)). We investigated the following sizes of *Lyot* stop: 1.00, 0.99, 0.98, 0.96, and 0.92 entrance pupil image. The interested reader will find in Appendix C the same study for the classical *Lyot* coronagraph.

These plots give an intuition of the behaviour of the result. Indeed, we show here that the *Lyot* stop mainly acts over the diffracted light in the range  $1.2$ – $3 R_\odot$ , and does not significantly impact the main diffraction feature. As shown in Fig. 12, reducing the radius of the *Lyot* stop from 1.00 to 0.99 already gives appreciable improvement on the rejection, of about one order of magnitude. In parallel, increasing the size of the internal occulter mainly contributes to reducing the level of residual sunlight around the edge of the external occulter image – Fig. 11. We observe an improvement of two orders of magnitude from 1.005 to 1.02 external occulter image. However, it seems that the performance in rejection in the range  $1.5$ – $3.2 R_\odot$  is more impacted by the size of the *Lyot* stop than the internal occulter. It is also interesting to observe that the position of diffraction peak matches the position of the image of the internal occulter in plane D. So, when increasing the size of the occulting mask, the peak of diffraction translates accordingly. As a result, the residual diffracted sunlight keeps contaminating the inner region of the field of view.

It is of course the combined effect of the internal occulter and the *Lyot* stop that makes the performance of the coronagraph. Figure 13 illustrates this point as we have plotted the residual diffracted sunlight level observed at  $1.3 R_\odot$ , versus the radius of the internal occulter and versus the radius of the *Lyot* stop. At that stage, one can already get an idea of possible theoretical performance (for an ideal and perfect instrument), of such a hybrid externally occulted *Lyot* solar coronagraph – in this particular configuration. At least, rejecting diffracted sunlight below  $10^{-8} B_\odot$  at  $1.3 R_\odot$  using a  $1.065 R_\odot$  internal occulter looks feasible, but this shall be considered as a theoretical lower limit.

#### 4.5. Analysis of the vignetting

Finally, we discuss the vignetting induced by both external and internal occulters since it is a characteristic feature in

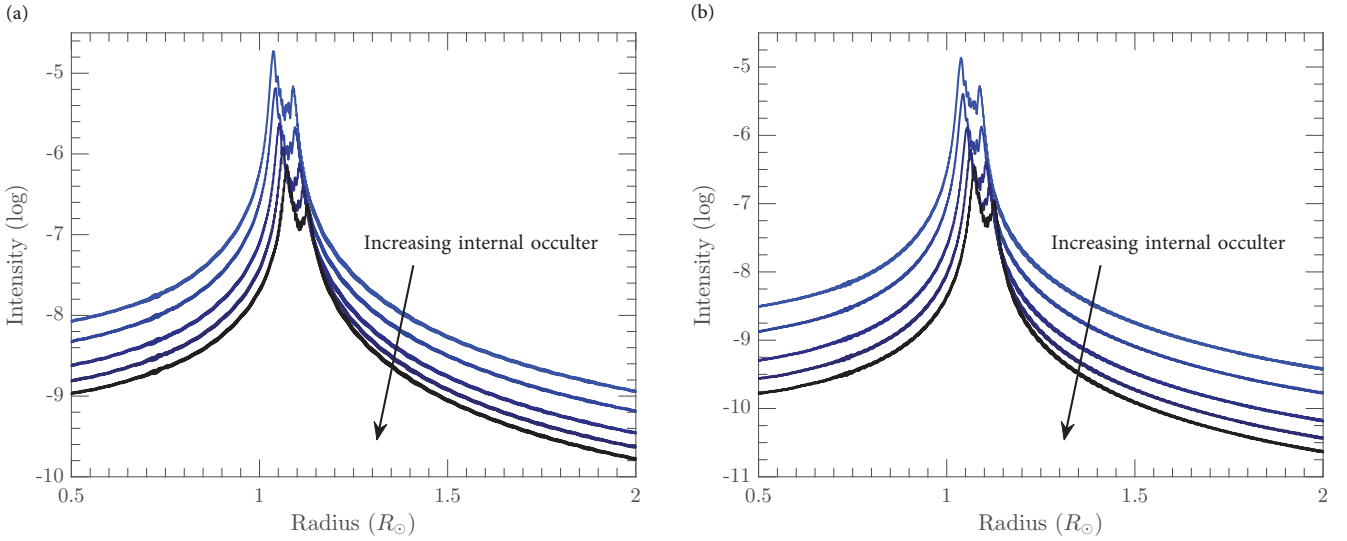


**Fig. 11.** Radial cuts  $I_D(r)$  for internal occulters of 1.005, 1.01, 1.02, 1.03 and 1.04 external occulter image, in logarithmic scale. **a)** Fixed Lyot stop of 0.99 entrance pupil image. **b)** Fixed Lyot stop of 0.96 entrance pupil image. The transverse radius is given in solar units, in the range  $[0.5 R_\odot, 2 R_\odot]$ . The intensities are normalized to the mean solar brightness.

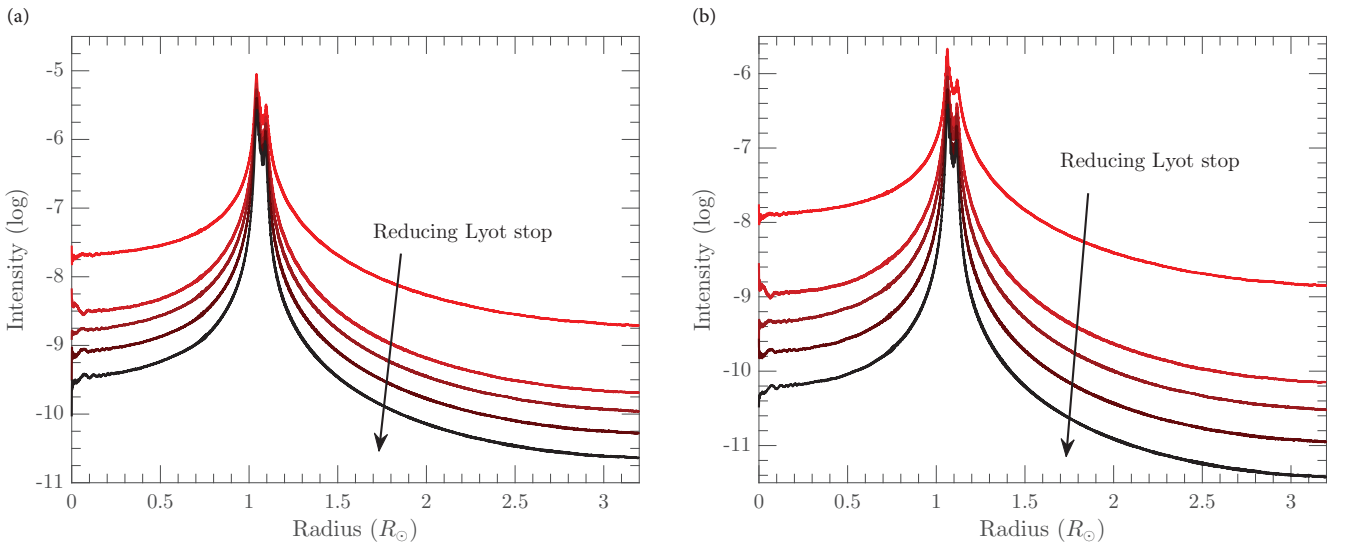


**Fig. 12.** Radial cuts  $I_D(r)$  for Lyot stops of 1.00, 0.99, 0.98, 0.96 and 0.92 radius, in logarithmic scale. **a)** Fixed internal occulter of 1.01 external occulter image. **b)** Fixed internal occulter of 1.03 external occulter image. The transverse radius is given in solar units. The intensities are normalized to the mean solar brightness.

coronagraphy. A dedicated analytic study of issues with external occultation can be found in [Raja Bayanna et al. \(2011\)](#). This vignetting affects the transition region where the coronagraph removes the direct light from the solar disc and transmits that of the solar corona. In our present study, we take advantage of our model of light wave propagation to estimate the vignetting coming from off-axis point sources outside the solar disc, that is,  $\rho = \sqrt{\alpha^2 + \beta^2} > R_\odot$ . Again, the complex amplitude  $\Psi_{A,\alpha,\beta}$  incoming into the entrance aperture is given by Eq. (3). It is interesting to understand the consequences of the external occultation. We remind the reader that the figure of the Arago bright spot in plane A, plotted in Fig. 2, is shifted of the quantity  $(z_0 \times \alpha, z_0 \times \beta)$  towards negative  $(x, y)$  directions. The transition between the shadow region and the high-intensity plateau is located around  $R = 710$  mm from the centre of the spot. Denoting  $\rho_{0\%} = (R - R_p)/z_0 = 1.0196 R_\odot = 979$  arcsec and

$\rho_{100\%} = (R + R_p)/z_0 = 1.094 R_\odot = 1050$  arcsec, we can roughly say that

$\rho \leq \rho_{0\%}$ : only faint diffracted light from the shadow region will enter the entrance pupil, corresponding to the occulted region of the sky;

$\rho_{0\%} \leq \alpha \leq \rho_{100\%}$ : the high-intensity plateau is partially captured by the entrance pupil. This region of the sky is partially vignitted;

$\alpha \geq \rho_{100\%}$ : the part of the wave front that enters into the entrance pupil is poorly affected by the external occulter and can be approximated by a planar tilted wave front. There is no vignetting.

The complete vignetting function of the coronagraph has been inspected by propagating the wave front from unitary amplitude point sources in the range  $\rho_{0\%} \leq \alpha \leq \rho_{100\%}$ , and  $\beta = 0$ . In Fig. 14

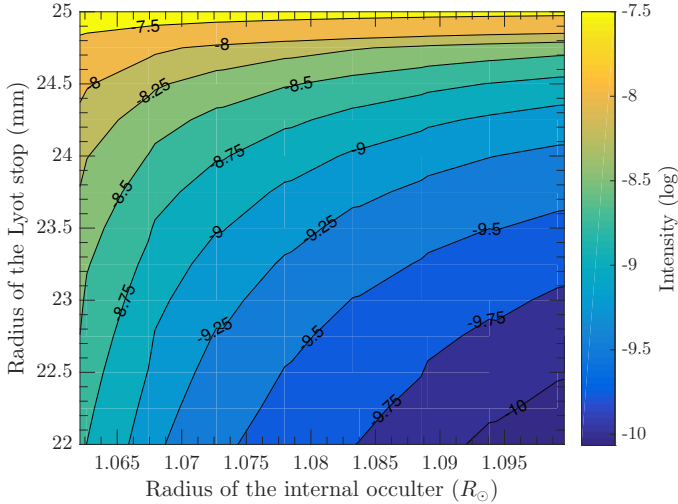


**Fig. 13.** Residual diffracted sunlight level at  $1.3 R_{\odot}$  for the hybrid externally occulted *Lyot* coronagraph  $S_{EL}$ , in logarithmic scale. The horizontal axis represents the radius of the internal occulter set in  $O'$ , in  $R_{\odot}$  units. The vertical axis represents the radius of the *Lyot* stop set in plane C, in millimeters units – 1: scale with respect to plane A.

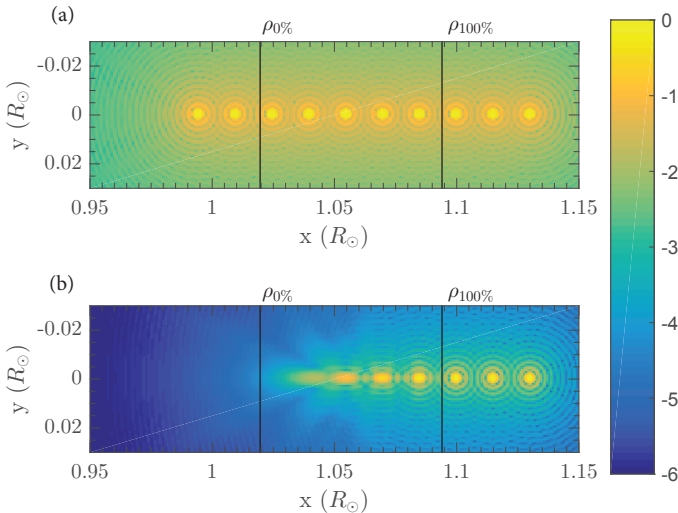


**Fig. 14.** Impulse response from unitary point sources in plane D, in logarithmic scale. The angular coordinates of the point sources are  $\beta = 0$  and, from left to right,  $\alpha = 0.995 R_{\odot}$ ,  $\alpha = 1.010 R_{\odot}$ ,  $\alpha = 1.025 R_{\odot}$ ,  $\alpha = 1.040 R_{\odot}$ ,  $\alpha = 1.055 R_{\odot}$ ,  $\alpha = 1.070 R_{\odot}$ ,  $\alpha = 1.085 R_{\odot}$ ,  $\alpha = 1.100 R_{\odot}$ ,  $\alpha = 1.115 R_{\odot}$  and  $\alpha = 1.130 R_{\odot}$ . **a)** Reference system without external and internal occulters. **b)** Complete system  $S_{EL}$ . The two vertical lines represent the limit of the fully vignetted zone  $\rho_{0\%}$  and the limit of the fully unvignetted zone  $\rho_{100\%}$ .

we plot the two-dimension observed intensities in plane D for the externally hybrid external *Lyot* coronagraph  $S_{EL}$ , using a  $1.065 R_{\odot}$  internal occulter and a  $0.99$  *Lyot* stop. Plot (a) represents the impulse responses when there is no external nor internal occulters. In that case, we observed perfect Airy patterns. Plot (b) illustrates the actual response of the coronagraphic system, i.e. with both occulters. We can see in Fig. 14 the strong nonlinear perturbation of the inner corona, in addition to the attenuation of the intensity. The image reconstruction in this region will be a delicate problem of inversion in a Fredholm regime. Beyond  $\rho_{100\%}$ , we find again a perfect Airy pattern, as expected.

## 5. Conclusions

We have presented a dedicated analytic and numerical analysis of the theoretical rejection performance of the classical *Lyot* coronagraph, the externally occulted solar coronagraph, and the hybrid externally occulted *Lyot* coronagraph. We first computed Fresnel diffraction produced by the external occulter, and second the coherent propagation of the wave fronts through the instrument. Here, our results applies to the geometry of ASPIICS coronagraph. We provide the observed intensity of residual sunlight in the final focal plane, that may contaminate the observation of the solar corona in white light, especially close to the solar limb. Using a *Lyot* mask of  $1.065 R_{\odot}$  radius and a *Lyot* stop being  $0.99$  times the image of the entrance aperture radius, we showed that the perfect classical *Lyot* coronagraph manages to reject below  $10^{-6} B_{\odot}$  from  $1.3 R_{\odot}$ . The externally occulted solar coronagraph provides a better performance, with a gain of one order of magnitude outside the diffraction peak intensity. Finally, the hybrid externally occulted *Lyot* coronagraph improves the global performance by rejecting diffracted sunlight below  $10^{-8} B_{\odot}$  from  $1.3 R_{\odot}$ . We also refined our study to exhibit the coupled effects of sizing both internal occulter and *Lyot* stop, in the case of the hybrid coronagraphic system. Oversizing the mask allows us to decrease the intensity of the diffraction peak intensity located around the image of the external occulter, and reducing the radius of the *Lyot* stop allows to globally reduce the residual sunlight. As a concrete result, we have provided in Fig. 13 a graph estimating the rejection at  $1.3 R_{\odot}$ , as a function of both sizes of the internal occulter and *Lyot* stop.

Rather than investigating whether the hybrid externally occulted *Lyot* solar coronagraph could meet any requirements in stray light rejection, our work claims to be a methodological model in order to estimate the end-to-end performance of such instruments. Solar astronomy will benefit from it to identify any benchmark for ongoing or future activities. However, we would like to emphasize that the given results remain a lower bound. In practice, performance would be degraded by any other sources of stray light and scattering.

As future activities, one can investigate in the nature of the external occulting disc itself. Radially apodized external occulters have already been analytically proved by Aime (2013) to be more efficient than the sharp-edged disc, in the context of solar coronagraphy. In an experimental approach, Bout et al. (2000) and Landini et al. (2010) investigated 3D-shaped occulters which deviate from a simple radial apodization. Model validation against experimental results would be very interesting and instructive. However, the main difficulty stands in the two-dimensional representation of such complex external occulter shapes and computing the Fresnel diffraction, as it has been recently investigated by Sirbu et al. (2016), in addition to the extend source that is represented by the Sun.

*Acknowledgements.* We would like to thank the European Space Agency and Proba-3 project for having supported this activity.

## References

- Aime, C. 2007, *A&A*, 467, 317
- Aime, C. 2013, *A&A*, 558, A138
- Aime, C., Soummer, R., & Ferrari, A. 2002, *A&A*, 389, 334
- Aschwanden, M. J. 2005, *Physics of the Solar Corona. An Introduction with Problems and Solutions*, 2nd edn. (Berlin: Springer)
- Born, M., & Wolf, E. 2006, in *Principles of Optics*, 7th edn. (Cambridge University Press), 484

- Bout, M., Lamy, P., Maucherat, A., Colin, C. & Llebaria, A. 2000, *Appl. Opt.*, **39**, 22
- Brueckner, G. E. Howard, R. A., & Koomen, M. J. et al. 1995, *Sol. Phys.*, **162**, 357
- Cash, W. 2006, *Nature*, **442**, 51
- Cox, A. N. 2000, *Allen's astrophysical quantities* (New York: AIP Press; Springer)
- Dollfus, A. 1983, *Astronomie*, **97**, 107
- Evans, J. W. 1948, *Space Sci. Rev.*, **47**, 95
- Ferrari, A. 2007, *ApJ*, **657**, 1201
- Ferrari, A., Aime, C., & Soummer, R. 2010, *ApJ*, **708**, 218
- Flamary, R., & Aime, C. 2014, *A&A*, **569**, A28
- Fort, B., Morel, C., & Spaak, G. 1978, *A&A*, **63**, 243
- Galy, C. 2015, *Proc. of SPIE*, **9604**, 96040
- Goodman, J. W. 2005, *Introduction to Fourier Optics* (Roberts and Company Publishers)
- Hamme, V. 1993, *ApJ*, **106**, 5
- Koutchmy, S. 1988, *Sci. Sci. Rev.*, **47**, 95
- Landini, F., Mazzoli, A., Venet, M., et al. 2010, *Proc. of SPIE*, **7735**, 77354
- Lemoine, D. 1994, *J. Chem. Phys.*, **101**, 3936
- Lenskii, A. V. 1981, *Astron. Zh.*, **58**, 648
- Lamy, P., Damé, L., Vivès, S., & Zukhov, A. 2010, *Proc. of SPIE*, **7731**, 18
- Lyot, B. 1939, *MNRAS*, **99**, 580
- Newkirk, G., Jr. & Bohlin, D. 1965, *Ann. Astrophys.*, **28**, 234
- Peter, H., Bingert, S., Klimchuk, J. A., et al. 2013, *A&A*, **556**, A104
- Purcell, J. D., & Koomen, M. J. 1962, in *Report of NRL Progress*, US GPO, Washington D. C., 9
- Raja Bayanna, A., Mathew, K., Sankarasubramanian, K., et al. 2011, *Exp. Astron.*, **29**, 145
- Renotte, E., Alia, A., Bemporad, A., et al. 2015, *Proc. of SPIE*, **9604**, 96040
- Sirbu, D., Kim, Y., Kasdin, N. J., & Vanderbei, R. J. 2016, *Appl. Opt.*, **55**, 22
- Soummer, R., Pueyo, L., Sivaramakrishnan, A., & Vanderbei, R. J. 2007, *Opt. Exp.*, **15**, 15935
- Vanderbei, R. J., Kasdin, N. J., & Cady, E. 2007, *ApJ*, **665**, 794
- Venet, M., Bazin, C., Koutchmy, S., & Lamy, P. 2010, *Proc. Int. Conf. Space Optics (ICSO 2010)*, held in Greece Oct. 2010, Session 9b
- Wolfram 2012, *Mathematica* (Champaign, IL: Wolfram Research, Inc.)
- Zhukov, A. N., Veselovsky, I. S., Koutchmy, S., & Delanné, C. 2000, *A&A*, **353**, 786

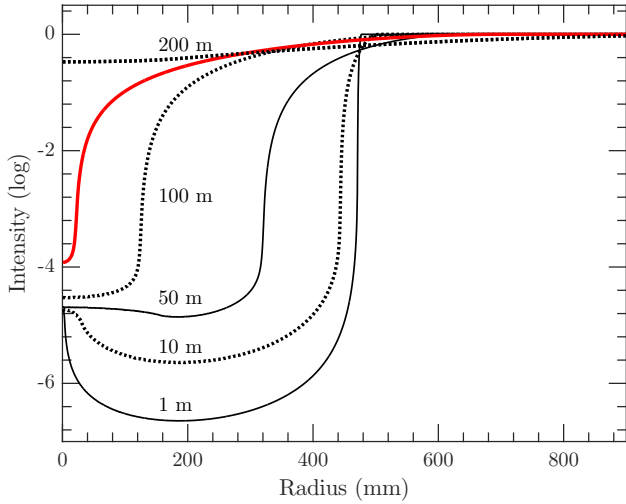


**Fig. A.1.** Intensity  $I_A(r)$  on plane A in a logarithmic scale. The intensity is normalized to the mean solar brightness. From top to bottom:  $z_0 = 1$  m, 10 m, 50 m, 100 m, 144.348 m and 200 m. The red curve corresponds to ASPIICS nominal geometry.

**Table A.1.** Distance  $z_0$  between the external occulter and plane A, stenope image radius of the Sun in plane O and geometrical radius of the umbra.

$z_0$	Solar stenope image	Geometrical umbra
1 m	4.65 mm	705 mm
10 m	46.5 mm	633 mm
50 m	233 mm	477 mm
100 m	465 mm	240 mm
144.348 m	672 mm	38 mm
200 m	931 mm	No umbra

## Appendix A: Study of the penumbra cone by varying the distance $z_0$

The shape of the umbra cone is intimately linked to the distance  $z_0$  between the external occulter and the telescope. In the context of Proba-3 Formation Flying mission, this is of particular interest, since the inter spacecraft distance separated the coronagraph and the occulter may vary. We computed the Fresnel diffraction pattern (Eq. (5)) and the penumbra profile  $I_A(r)$  in plane A (Eq. (12)) for different values of  $z_0$ , while keeping a constant radius  $R$  for the external occulter.

In Fig. A.1, we give the radial penumbra profile of diffracted sunlight in logarithmic scale at  $z_0 = 1$  m, 10 m, 50 m, 100 m, 144.348 m and 200 m. First of all, we must state that Fresnel diffraction theory usually requires small angles approximation, which may not be the case at small  $z_0$ . The smaller  $z_0$ , the smaller the stenope image of the Sun in plane O, computed as  $z_0 \tan R_\odot$ , as given in Table A.1. From  $z_0 \leq 50$  m, we observe that the penumbra is bell-shaped in the central region. This comes from the two-dimension convolution of this stenope image with the

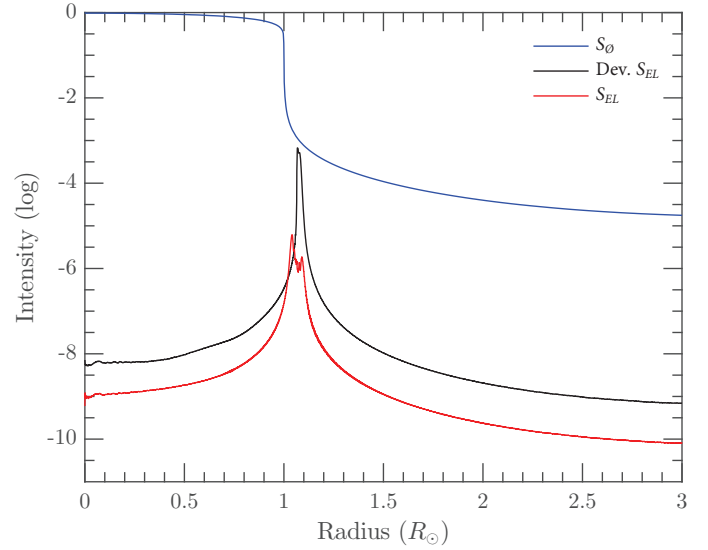


**Fig. B.1.** Observed intensities in the focal plane, in logarithmic scale. The transverse radius is given in solar units. The intensities are normalized to the mean solar brightness. Blue: system  $S_\emptyset$  given by  $I_B(r)$  in plane B, as reference. Black: deviation from system  $S_{EL}$ , with the internal occulter set in plane B, given by  $I_D(r)$  in plane D. Red: system  $S_{EL}$ , with the internal occulter set in plane O', given by  $I_D(r)$  in plane D.

Arago bright spot in plane A. At larger  $z_0$ , this feature vanishes and we obtain a smooth penumbra profile. We notice that the umbra is about 2,5 darker at  $z_0 = 100$  m than 144.348 m, as plane A is then closer to the occulter. The geometrical umbra is reduced to a point at  $z_0 = 152.55$  m, and the so-called ante-umbra region extends behind, where the external occulter cannot mask the whole solar disc any more. This last case is illustrated by  $z_0 = 200$  m in Fig. A.1.

## Appendix B: Comparing planes B and O' for the internal occulter in system $S_{EL}$

This Appendix completes the discussion in Sect. 4.3.4 about the position of the internal occulter in the hybrid externally occulted *Lyot* coronagraph  $S_{EL}$ . We investigate the case where the internal occulter is set in plane B instead of plane O'. In Fig. B.1, we compare the final observed intensities  $I_D(r)$  in plane D between the system  $S_{EL}$  and its deviation (both plotted in the figure) which has the internal occulter set in plane B. The results are normalized to the reference system  $S_\emptyset$  (also plotted). In both cases, the internal occulter has a radius of  $1.065 R_\odot$  and the *Lyot* stop sizes 0.99 times the image of the entrance pupil in plane C.

Of course, setting the internal occulter in plane O' instead of plane B is much more efficient about stray light rejection, as already discussed in Sect. 4.3.4. We observe an average gain in performance of one order of magnitude. The diffraction peak intensity around  $1.06 R_\odot$  is even two orders of magnitude lower.

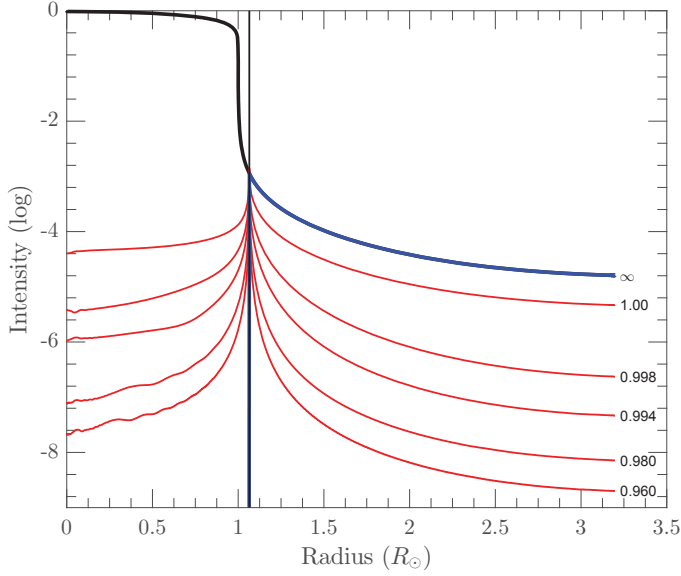


**Fig. C.1.** Radial cuts  $I_D(r)$  for the classical *Lyot* coronagraph  $S_L$ , in logarithmic scale. The transverse radius is given in solar units. Intensities are normalized to the mean solar brightness. Black: raw image of the Sun. Blue: infinite *Lyot* stop. Red: *Lyot* stop of 1.00 (25 mm), 0.998 (24.95 mm), 0.994 (24.85 mm), 0.980 (24.5 mm), and 0.960 (24 mm) radius, from top to bottom respectively. Vertical line: 1.065  $R_\odot$  radius *Lyot* mask.

### Appendix C: Reducing the *Lyot* stop for the classical *Lyot* coronagraph

We report in this appendix the impact of reducing the *Lyot* stop for the classical *Lyot* coronagraph  $S_L$ . The approach is the same as the one presented in Sect. 4.4. We computed the global response in the final focal plane by varying the radius of the *Lyot* stop, from 1.00 to 0.96 times the image of the entrance pupil, and using a fixed 1.065  $R_\odot$  *Lyot* mask set in plane B. Figure C.1 shows the results  $I_D(r)$ . The reader can clearly appreciate the gain of reducing the *Lyot* stop. We also investigated the case without *Lyot* stop in plane C, that is, an infinite radius. We observe no rejection in this last case, and plane D corresponds to the exact image of plane B.

## Appendix D: Two-dimension intensities

In this appendix, we report the two-dimension image of the global response for the four different imaging systems studied. In Fig. D.1 we plotted  $I_B(x, y)$  in plane B for the raw telescope  $S_\emptyset$  and the external coronagraph  $S_E$ , and  $I_D(x, y)$  in plane D for

the classical *Lyot* coronagraph  $S_L$  and the hybrid externally occulted *Lyot* coronagraph  $S_{EL}$ . A  $1.065 R_\odot$  radius *Lyot* mask or internal internal and a  $0.99$  radius *Lyot* stop have been used for the computation. The same colour logarithmic scale has been set to every plots for a purpose of direct comparisons.

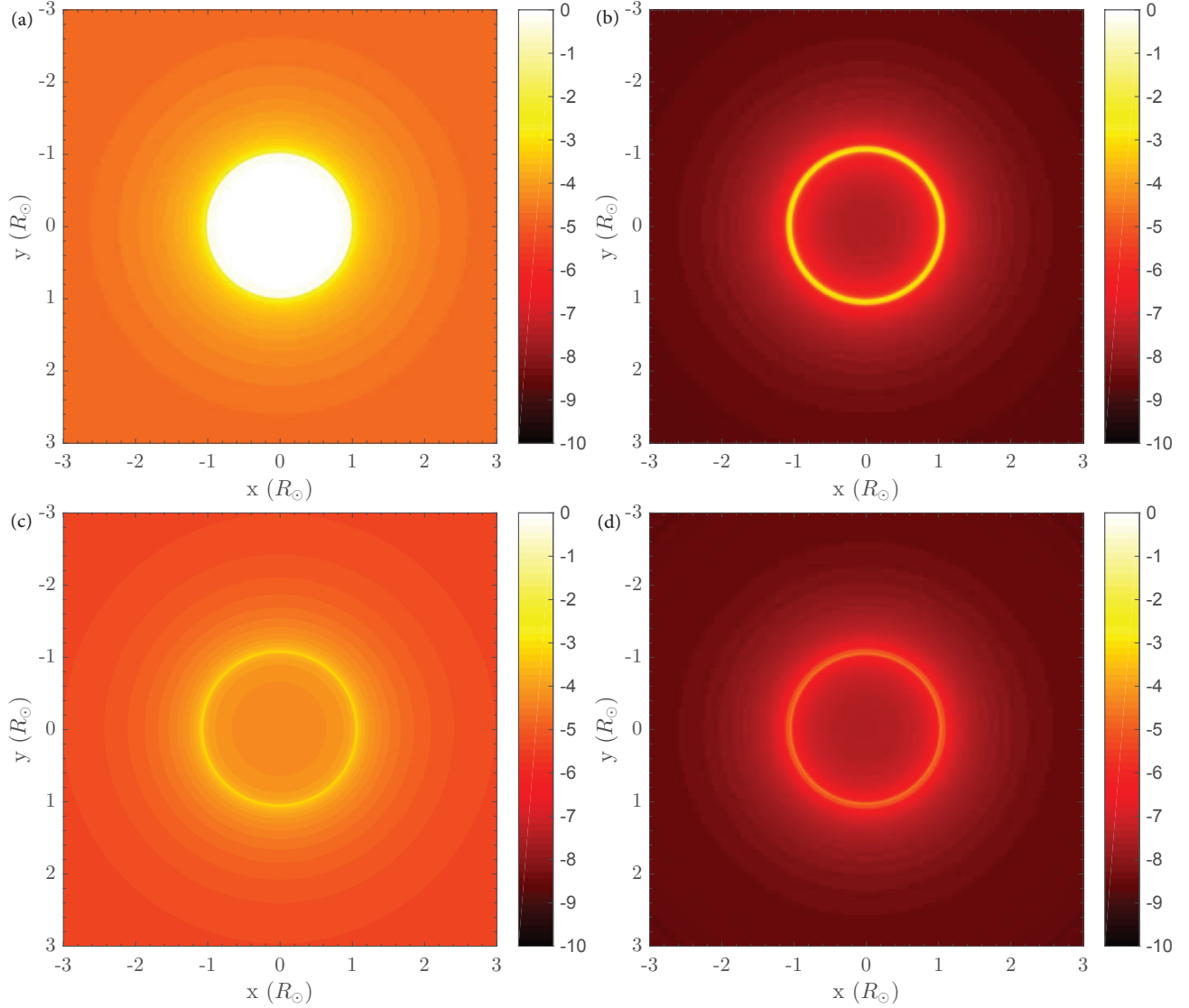


**Fig. D.1.** Two-dimension final response as observed intensities in the detection plane, in logarithmic scale. The intensities are normalized to the mean solar brightness. **a)**  $I_B(x, y)$  for system  $S_\emptyset$ . **b)**  $I_B(x, y)$  for system  $S_E$ . **c)**  $I_D(x, y)$  for system  $S_L$ . **d)**  $I_D(x, y)$  for system  $S_{EL}$ .